



Provided by the author(s) and University of Galway in accordance with publisher policies. Please cite the published version when available.

Title	Exploiting tissue dielectric properties to shape microwave thermal ablation zones
Author(s)	Bottiglieri, Anna; Ruvio, Giuseppe; O'Halloran, Martin; Farina, Laura
Publication Date	2020-07-16
Publication Information	Bottiglieri, Anna, Ruvio, Giuseppe, O'Halloran, Martin, & Farina, Laura. (2020). Exploiting Tissue Dielectric Properties to Shape Microwave Thermal Ablation Zones. <i>Sensors</i> , 20(14), 3960. doi:10.3390/s20143960
Publisher	MDPI
Link to publisher's version	<a href="https://doi.org/10.3390/s20143960">https://doi.org/10.3390/s20143960</a>
Item record	<a href="http://hdl.handle.net/10379/16630">http://hdl.handle.net/10379/16630</a>
DOI	<a href="http://dx.doi.org/10.3390/s20143960">http://dx.doi.org/10.3390/s20143960</a>

Downloaded 2024-04-26T05:26:37Z

Some rights reserved. For more information, please see the item record link above.



1 Article

## 2 Exploiting tissue dielectric properties to shape 3 microwave thermal ablation zones

4 Anna Bottiglieri <sup>1,2,\*</sup>, Giuseppe Ruvio <sup>2,3</sup>, Martin O'Halloran <sup>2,\*</sup> and Laura Farina <sup>2,4</sup>

5 <sup>1</sup> Electrical and Electronic Engineering, National University of Ireland Galway, Galway, Ireland;

6 <sup>2</sup> Translational Medical Device Lab, National University of Ireland Galway, Ireland;

7 <sup>3</sup> Endowave Ltd. National University of Ireland Galway, Ireland;

8 <sup>4</sup> CÚRAM, SFI Research Centre for Medical Devices, Galway, Ireland;

9 \* Correspondence: [a.bottiglieri1@nuigalway.ie](mailto:a.bottiglieri1@nuigalway.ie) (A.B.); [martin.ohalloran@nuigalway.ie](mailto:martin.ohalloran@nuigalway.ie) (M.O.)

10 Version June 3, 2020 submitted to Sensors

11 **Abstract:** The dielectric characterization of tissue targets of microwave thermal ablation (MTA) have  
12 improved the efficacy and pre-procedural planning of treatment. In some clinical scenarios the tissue  
13 target lies at the interface with an external layer of fat. The aim of this work is to investigate the  
14 influence of the dielectric contrast between fat and target tissue on the shape and size of the ablation  
15 zone. A 2.45 GHz monopole antenna is placed parallel to an interface modelled by fat and a tissue  
16 characterized by higher dielectric properties and powered at 30W and 60W for 60s. The performances  
17 of MTA are numerically investigated considering different interface scenarios (i.e. different widths  
18 of fat layer, shifts in the antenna alignment) and a homogeneous reference scenario. Experiments  
19 (N=10) are conducted on *ex vivo* porcine tissue to validate the numerical results. Asymmetric heating  
20 patterns are obtained in the interface scenario; the ablation zone in the target tissue is **two-fold to ten-**  
21 **fold** the size of the zone in the adipose tissue, and up four times larger than the homogenous scenario.  
22 The adipose tissue reflects the electromagnetic energy into the adjacent tissue target reducing the  
23 heating in the opposite direction.

24 **Keywords:** Microwave ablation, directional heating pattern, biological tissue interface,  
25 electromagnetic therapeutics, targeted ablation therapy

26

### 27 1. Introduction

28 Microwave thermal ablation (MTA) is an alternative therapeutic technique for the treatment of  
29 tumors in patients who are not surgical candidates [1-3]. In MTA, diseased tissues are destroyed by  
30 inducing a high and focused temperature increase (above 55 °C) [4,5]. Localized heating is achieved  
31 through tissue absorption of the electromagnetic (EM) energy, at microwave (MW) frequencies [6].  
32 In MTA, the EM field is radiated by an antenna typically powered at 915 MHz or 2.45 GHz [1,7]. The  
33 treatment protocol is based on defining the power and time settings of the EM field radiated by the  
34 antenna to obtain the desired thermal lesion (i.e. ablation zone) [8]. The clinical objective is to achieve  
35 ablative temperatures (at least 55 °C) in the target tissue, while sparing the surrounding healthy  
36 tissues [1-5]. Promising results of MTA have been reported for the treatment of hepatocellular  
37 carcinomas [9,10], hepatic metastases [11], renal tumors [12,13], lung tumors [14] and bony lesions  
38 [15].

39 Recent studies have presented MTA applicators capable of creating directional patterns to  
40 achieve energy deposition limited to preferred directions [16-18]. In particular, reflector-based MTA  
41 antennas equipped with a variety of reflector shields have been proposed. In [16], a monopole  
42 antenna equipped with a hemi-cylindrical reflective shield is described. In [18], two different ablation  
43 devices equipped with spherical and parabolic reflectors are proposed. Promising results were  
44 obtained on *ex vivo* bovine liver in terms of localized directional energy deposition. Such MTA

45 applicators have been proposed to meet specific clinical scenarios requiring a side-firing approach.  
46 Preservation of healthy tissues around the target region (e.g. diaphragm in peripheral liver lesions  
47 [19], spinal cord in metastatic spinal bone tumours [20]) and sparing blood vessels (e.g. renal artery,  
48 renal vein, inferior vena cava) are crucial clinical goals to ensure patient safety. However, directional  
49 applicators require to be carefully oriented to the target by the surgeon; this procedure is not easy to  
50 perform under conventional 2D imaging guidance.

51 In this work, we investigate an alternative strategy to focus the radiation energy in a target  
52 region by exploiting the typical presence of fat around the target to direct the EM energy. This side-  
53 firing approach can be adopted in any peripheral anatomical target surrounded by a layer of visceral  
54 fat (like subcapsular hepatic lesions, exophytic renal tumors or adreno-cortical adenomas) using any  
55 omnidirectional antenna, hence no orientation by the surgeons is required. Any fat interface is clearly  
56 visible through imaging techniques and can be easily adopted to align the MTA applicator, and thus  
57 the EM beam, under the guidance of imaging systems currently used in MTA (e.g. CT and  
58 ultrasound). The interaction between the EM field and the targeted tissue is strictly related to the  
59 water content in each tissue, and thus to the dielectric properties (i.e. relative permittivity and  
60 effective conductivity) of the biological tissue [21].

61 The relative permittivity is a function of the ability of the tissue to store energy when an external  
62 electric field is applied. The effective conductivity indicates the dissipative nature of the tissue, which  
63 absorbs the energy from the applied electric field and partially convert it to heat. The higher the  
64 values of relative permittivity and effective conductivity of the tissue, the higher are the capabilities  
65 of the tissue to store, absorb and convert the applied EM energy to heat. The relative permittivity and  
66 effective conductivity gradient lying at the interface between fat ( $\epsilon_r = 10.8$ ,  $\sigma = 0.3$  S/m at 2.45 GHz)  
67 and other tissues can be used to direct the EM radiation and the consequent rise of temperature to  
68 the desired target [22-24]. As an example, liver, kidney and adrenal glands are characterized by  
69 dielectric properties values three to eight times higher than fat. Relative permittivity of liver tissue is  
70 about four times that of fat tissue; while in kidney and adrenal gland the multiplicative factor is five  
71 and six respectively. Effective conductivity of fat is instead four times lower than adrenal gland, about  
72 six times lower than liver and about eight times lower than kidney. In this study, muscle and fat  
73 tissues were adopted to investigate the effect of the dielectric contrast on the shaping of the ablation  
74 zone. Compared to the above-mentioned clinical targets, muscle represents a conservative model:  
75 relative permittivity and effective conductivity of muscle are four and three times higher than fat, i.e.  
76 the dielectric contrast is smaller compared to liver, kidney or adrenal gland.

77 A comprehensive proof-of-concept study including both numerical and experimental  
78 evaluations was conducted to validate the feasibility of exploiting the fat layer to purposely and  
79 effectively direct the ablation zone. In the numerical study, the fat and muscle tissues were modelled  
80 by two layers represented by the corresponding dielectric properties acquired at room temperature.  
81 The results obtained in the two-layers scenario were compared with a homogeneous scenario, to  
82 highlight the asymmetry obtained. An interstitial MTA monopole antenna was designed and  
83 optimized for the study. The numerical tests were experimentally validated: the designed antenna  
84 was built and *ex vivo* experiments were conducted exploiting the natural interface between fat and  
85 muscle using porcine tissue samples.

86 The remainder of this work is organized as follows: Section II describes the numerical and the  
87 experimental methodology. In Section III, the results in terms of antenna performance and  
88 temperature distributions are shown. In Section IV, the results obtained are discussed, comparing the  
89 numerical and experimental outcomes in terms of the temperature distributions. Finally, in Section  
90 V, the conclusions of this work are presented.

## 91 2. Materials and Methods

### 92 3.1. Numerical Study

93 An 18-gauge monopole antenna was modelled using a 3-D (three dimensional) commercial full-  
94 wave electromagnetic software (CST MWS Suite 2018, Darmstadt, Germany). A simulation-based

95 approach involving a parametric sweep across the range of 0.5 - 3 GHz was employed to optimize  
 96 the length of the radiating element in order to obtain the minimum reflection coefficient (S11) for the  
 97 operating frequency of 2.45 GHz. A diagram of the designed applicator is depicted in Figure 1(a);  
 98 two concentric polyimide tubes were used to model an integrated cooling system. The water flow  
 99 proximal to the antenna radiating element allowed heat dissipation within the lossy cables, limiting  
 100 heating within and close to the applicator length. Convective boundary conditions along the feeding  
 101 cable of the antenna were considered to model the cooling system of the antenna: the convection  
 102 coefficient was set equal to 1000 ( $\text{W m}^{-2}\text{ }^{\circ}\text{C}^{-1}$ ) and the water temperature equal to 18  $^{\circ}\text{C}$ .

103 The above-mentioned CST MWS commercial software was used to conduct coupled  
 104 electromagnetic and thermal simulations. Firstly, a numerical study was conducted in a  
 105 homogeneous muscle scenario, and followed then a more complex interface scenario. The ablation  
 106 applicator was placed parallel to the interface between two biological tissues (i.e. fat and muscle) as  
 107 sketched in Figure 1(b). In the homogeneous scenario, the applicator was placed at the center of a  
 108 muscle-mimicking 3D geometry ( $x = 60 \text{ mm}$ ,  $y = 60 \text{ mm}$ ,  $z = 60 \text{ mm}$ ). For the interface scenario, a  
 109 multilayer 3D geometry was developed including two adjacent cuboids mimicking muscle and fat  
 110 dielectric tissues, characterized respectively by high and low dielectric properties values. The muscle  
 111 layer was 30 mm wide, whereas the fat was modelled by a 10 mm wide layer. The influence of the fat  
 112 layer width was investigated considering two scenarios where the width of the fat layer was  
 113 increased up to 15 mm and reduced to 5 mm. The influence of the antenna alignment was investigated  
 114 by shifting the antenna position of 1.5 mm both in muscle and in fat along the x-axis, with reference  
 115 to the initial position shown in Figure 1(b).

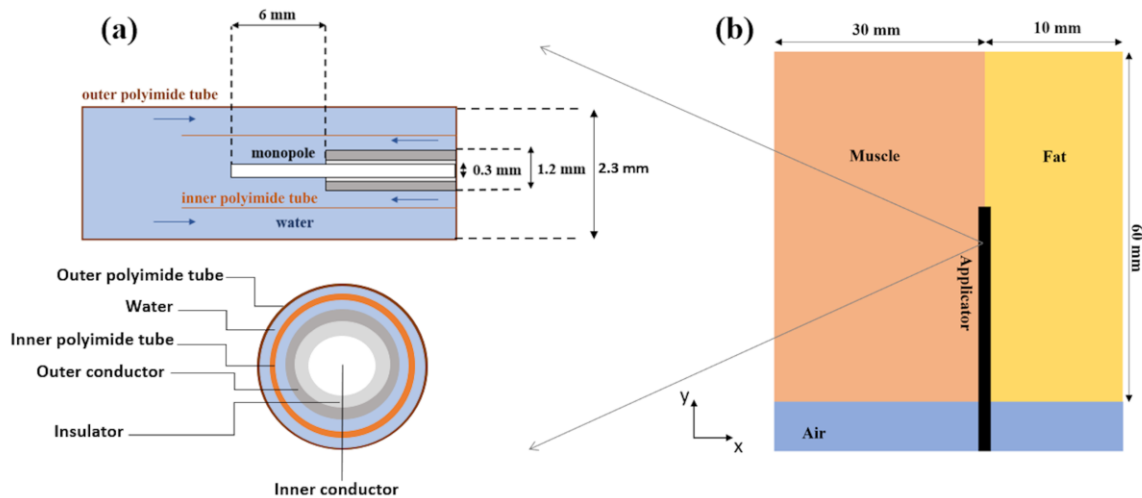


Figure 1: (a) Longitudinal-section (top) and cross-section (bottom) geometry of the distal portion of the interstitial MW antenna: the 6 mm radiating element and the integrated cooling system are depicted; the inbound and outbound water flows are illustrated (blue arrows). Both the inner tube, that provides the onward water flow, and the outer wall of the catheter are made of polyimide material; (b) Scheme of the applicator (MW antenna) placed parallel to the interface between two materials (muscle and fat) characterised by different dielectric and thermal properties.

116 The software solves the Helmholtz electromagnetic wave equation  
 117

$$\nabla^2 \mathbf{E} - k_0^2 \left( \epsilon_r - \frac{j\sigma}{\omega \epsilon_0} \right) \mathbf{E} = 0 \quad (1)$$

118 where  $\mathbf{E}$  ( $\text{V m}^{-1}$ ) is the electric field,  $k_0$  ( $\text{m}^{-1}$ ) the wave-number in the free-space,  $\epsilon_r$  the relative  
 119 permittivity,  $\sigma$  ( $\text{S m}^{-1}$ ) the effective conductivity,  $\omega$  ( $\text{rad s}^{-1}$ ) the angular frequency and  $\epsilon_0$  ( $\text{F m}^{-1}$ ) is the  
 120 permittivity of the free-space.

121 From the electromagnetic simulation, the specific absorption rate (SAR) distribution in the tissue  
 122 is calculated using (2)  
 123

$$SAR = \frac{\sigma |E|^2}{2\rho} \quad (2)$$

124 where  $\sigma$  (S m<sup>-1</sup>) is the effective conductivity,  $E$  (V m<sup>-1</sup>) the intensity of the electric field and  $\rho$  (kg m<sup>-3</sup>)  
 125 the density.

126 Then, Pennes' bioheat equation [25] is employed to describe the heat transfer inside the model  
 127 and to predict the resulting temperature distribution in the tissue  
 128

$$\rho c \frac{\partial T}{\partial t} = \nabla \cdot (k \nabla T) + \rho Q + \rho SAR - m_b c_b (T - T_b) \quad (3)$$

129 where  $\rho$  (kg m<sup>-3</sup>) is the density of the biological tissue,  $c$  (J kg<sup>-1</sup> K<sup>-1</sup>) the heat capacity of the tissue,  $T$   
 130 (K) the temperature,  $t$  (s) the time,  $k$  (W K<sup>-1</sup> m<sup>-1</sup>) the thermal conductivity of the biological tissue,  $Q$   
 131 (W kg<sup>-1</sup>) the metabolic heat generation rate, SAR (W kg<sup>-1</sup>) the rate of absorption of the electromagnetic  
 132 power by the biological tissues,  $m_b$  (kg m<sup>-3</sup> s) the blood mass perfusion rate,  $c_b$  heat capacity of the  
 133 blood and  $T_b$  is the temperature of the blood. The *ex vivo* condition was obtained in Equation 3  
 134 discarding the contribution of the metabolic heat ( $\rho Q$ ) and the blood perfusion ( $m_b c_b (T - T_b)$ ).

135 Scattering boundary conditions were applied to the outer surface of the modelled region to  
 136 minimize the reflected EM waves. The models were meshed in order to have denser mesh in the  
 137 regions with higher permittivity. **First a minimum meshing size was considered (i.e. ten cells per**  
 138 **wavelength), then the number of cells per wavelength was increased until a discrepancy in the S11**  
 139 **values less than 0.1% was obtained between two consecutive simulations.** Finally, the tissue models  
 140 were discretized using tetrahedrons with a size between 0.2 mm and 3.3 mm.

141 The thermal and dielectric properties used for the tissue models are detailed in Table 1 at 2.45  
 142 GHz. The dielectric properties were obtained experimentally and loaded into the material library of  
 143 the CST MWS software: measurements were conducted on *ex vivo* porcine tissue using a Keysight  
 144 slim form probe (N1501A) connected to a Keysight E5063A network analyzer (operating frequency  
 145 range: 100 kHz – 8.5 GHz) as described in [26]. The values related to heat capacity, thermal  
 146 conductivity and density were obtained from the literature [22] and manually loaded into the  
 147 material settings of the CST MWS software.

148 For the tissue models, the starting temperature was set to 25 °C. The effect of two power levels  
 149 commonly used [23,18] were compared over 60 s: 30 W and 60 W.

Table 1: Tissue dielectric and thermal properties employed in the numerical simulations.

Parameter	Fat	Muscle
Relative permittivity, $\epsilon_r$	8.7	41.0
Effective conductivity, $\sigma_{\text{eff}}$ [S/m]	0.1	0.7
Volumetric heat capacity, $\rho c$ [kJm <sup>-3</sup> K <sup>-1</sup> ]	2139	3729
Thermal conductivity, $k$ [Wm <sup>-1</sup> K <sup>-1</sup> ]	0.2	0.5
Frequency [GHz]	2.45	

150 The values obtained from each numerical simulation were exported and analyzed in MATLAB  
 151 (R2017a, The MathWorks, Inc., Natick, MA, US); **the error introduced for the representation of the**  
 152 **ablation profiles is around 0.1%.**

### 153 3.2. Experimental Study

154 The designed monopole antenna was then fabricated exposing 6 mm from the inner conductor  
155 of a UT-047 semirigid coaxial cable (Micro-Coax Inc., Pottstown, PA, US). A SMA connector was  
156 placed at 165 mm from the antenna feed-point [27].

157 The impedance matching of the fabricated antenna was evaluated in terms of reflection  
158 coefficient (S11) by connecting the antenna to an antenna analyzer (Rohde & Schwarz® ZVH8 100  
159 kHz – 8 GHz) through a coaxial cable. A full one-port calibration procedure was performed,  
160 considering three different calibration standards: open circuit, short circuit and 50  $\Omega$  load. Five  
161 measurements were conducted loading the test device (ablation antenna) with water at room  
162 temperature. The S11 values were recorded at 201 linearly spaced frequency points over 0.5 – 3 GHz.

163 After this preliminary step, experiments were conducted on *ex vivo* porcine tissue to validate the  
164 results of the numerical study. The temperature of the material under test (porcine tissue) was  
165 measured using an infrared thermometer (Fluxe 62 Max IR Thermometer, -30°C–500°C temperature  
166 range, accuracy of 1.5°C of reading at temperature  $\geq 0^\circ\text{C}$ ). The applicator was placed along the  
167 interface between fat and muscle layers and covered by another layer of tissue characterized by the  
168 same pattern. Two power and time settings were experimentally considered: 30 W for 60 s and 60 W  
169 for 60 s. The ablations were conducted with 32 W and 64 W as output powers at the microwave  
170 generator (Sairem, SAS, France) at 2.45 GHz.

171 The selected powers correspond to 30 W and 60 W at the antenna feed point, considering 1.9  
172 dB/m losses calculated along the coaxial cable with reference to the cable datasheet [28]. Five ablations  
173 were conducted for each setting, yielding a total of ten experiments. A peristaltic dispensing pump  
174 (DP2000, Thermo-Fisher Scientific Inc., Waltham, Massachusetts, US) was connected to the inflow  
175 channel of the ablation applicator, operating at 50 ml/min. For each experiment, the temperature was  
176 monitored using three fiber optic sensors (Neoptix Inc., Québec, CA) placed at three different  
177 distances from the antenna axis (reference axis) in correspondence with the antenna feed. Two fiber  
178 optic sensors were placed at a radial distance of 4 mm from the antenna feed in the muscle tissue and  
179 in the fat tissue, in order to consider the increase of the temperature caused by the direct heating in  
180 proximity to the antenna. One fiber optic sensor was placed at 7 mm from the antenna feed in the  
181 muscle, in order to account for the heat transfer by diffusion phenomena through the tissue (i.e.  
182 muscle) at a higher distance from the antenna feed. At  $t=0$  s the power supply from the MW generator  
183 was switched on; the temperature was monitored over 60 s.

### 184 3. Results

185 The MTA antenna performance was evaluated in terms of magnitude of the reflection coefficient  
186 (S11) and resonance bandwidth within the 0.5 – 3 GHz frequency range, numerically as well as  
187 experimentally, in water. The reflection coefficient of the antenna is equal to -12.6 dB and -22.4 dB at  
188 2.45 GHz for experimental and numerical results, respectively. A comparable -10 dB antenna  
189 bandwidth is obtained between 1.9 GHz and 2.5 GHz experimentally, and between 1.8 GHz and 2.9  
190 GHz numerically.

191 The numerical results related to different tissue models and antenna placements are illustrated  
192 in Figure 2 to 5; the thermal distributions achieved after 60 s in each tissues model are mapped for  
193 both the power settings considered, i.e. 30 W and 60 W. Two temperature profiles are highlighted: a  
194 contour line at 55°C marks the area where instantaneous coagulation occurs (i.e. ablation zone), while  
195 the 90°C contour line indicates the area where water vaporization in the tissue may occur [29-31].

196

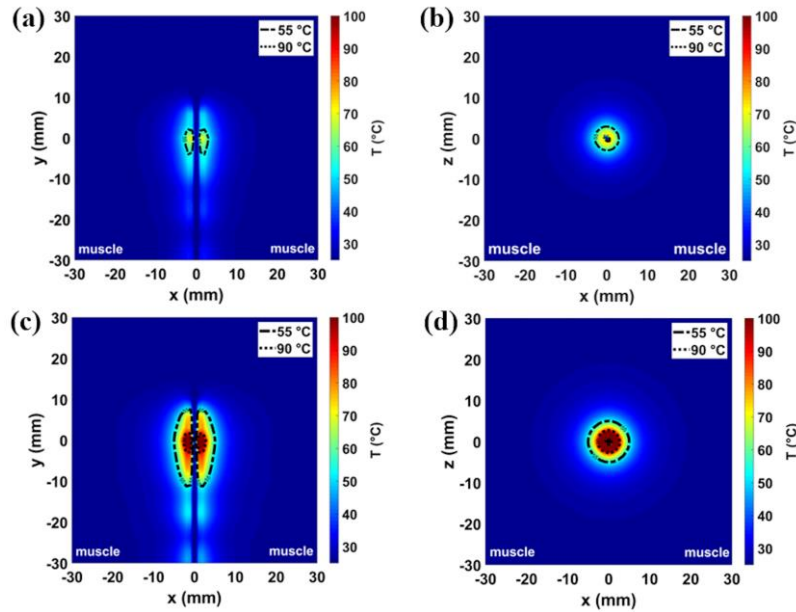


Figure 2: Simulated temperature patterns in the homogeneous muscle scenario shown both in a coronal plane (first column) and transverse plane (second column) with reference to the antenna feed. Two different power-time settings are reported: 30 W- 60s (a,b); 60W- 60s (c,d). The dash-and-dot lines represent 55°C boundary and the dot lines represent 90°C boundary.

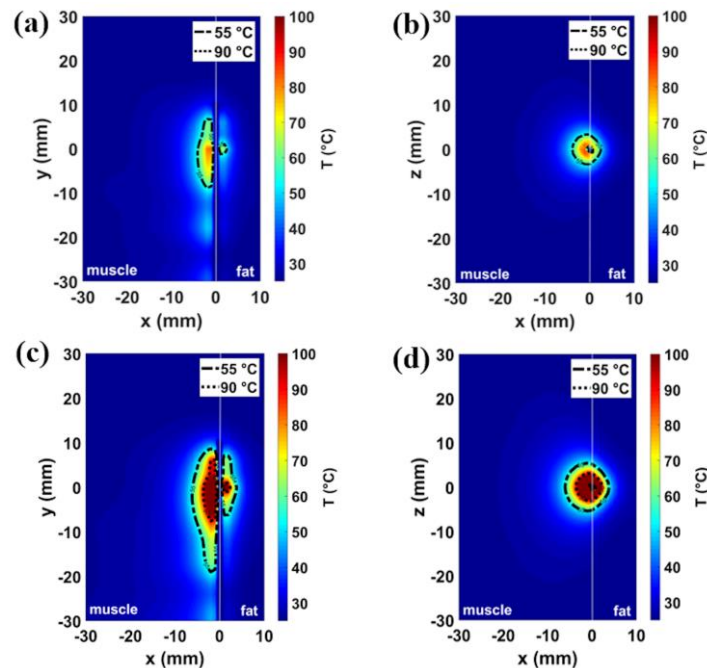


Figure 3: Simulated temperature patterns in muscle-fat interface scenario shown both in a coronal plane (first column) and transverse plane (second column) with reference to the antenna feed. Two different power-time settings are reported: 30 W- 60s (a,b); 60W- 60s (c,d). The dash-and-dot lines represent 55°C boundary and the dot lines represent 90°C boundary.

197 Figure 2 and Figure 3 show the temperature profiles obtained in the homogeneous muscle model  
 198 and in the muscle-fat interface model (10 mm fat layer), respectively. In particular, the temperature  
 199 profiles related to settings of 30 W for 60 s and 60 W for 60 s settings are depicted in figures (a-b) and  
 200 in figures (c-d), respectively. The asymmetry introduced by the inhomogeneity of the tissue (Figure

201 3) with respect to the homogeneous muscle scenario (Figure 2) can be observed. For the low power  
 202 setting (30 W for 60 s), the increase of temperature in the tissue close to the antenna is below 90 °C  
 203 both in the homogenous scenario of Figure 2(a-b) and in the interface scenario of Figure 3(a-b). The  
 204 area enclosed in the 55°C contour is 10 mm<sup>2</sup> each side (20 mm<sup>2</sup> overall) in the case of homogeneous  
 205 scenario; whereas in the case of the interface scenario, the extent of the area exceeding 55°C is 3 mm<sup>2</sup>  
 206 in fat and 41 mm<sup>2</sup> in muscle. Increasing the input power (60 W for 60 s), the MW heating affects larger  
 207 areas both in muscle homogeneous and in muscle-fat interface scenario, as shown in Figure 2(c-d)  
 208 and 3(c-d) respectively. In the case of 60 W setting, temperatures higher than 90°C are found in  
 209 proximity to the antenna feed both in the homogeneous muscle and muscle-fat interface scenarios.  
 210 However, temperature values exceeding 90 °C result in a smaller area in fat (< 3 mm<sup>2</sup>) compared to  
 211 the muscle (< 30 mm<sup>2</sup>) in the case of muscle-fat interface model. The area exceeding 55°C is around  
 212 65 mm<sup>2</sup> each side (130 mm<sup>2</sup> overall) in the homogeneous muscle model; whereas in the interface  
 213 scenario, they are approximately 31 mm<sup>2</sup> and 117 mm<sup>2</sup>, in fat and in muscle respectively. Comparing  
 214 the two settings, we can observe that the ablation area in muscle in the interface scenario at 30 W is  
 215 about ten times greater than the zone area in fat and four times the zone area in muscle (one side)  
 216 the homogeneous scenario; while in the interface case at 60 W, the ablation area in muscle is about  
 217 four times the zone area in fat and two times the zone area in muscle in the homogeneous case.

218 Figure 4 shows the impact of the fat layer width on the profiles of the ablation zone: the  
 219 temperature distributions obtained in the presence of 5 mm and 15 mm wide fat layers are illustrated  
 220 for the two different settings proposed (30 W in Figure 4(a-b) and 60 W in Figure 4(c-d)). No  
 221 significant variations in the extent of the ablation zone compared to the scenario of 10 mm fat layer  
 222 are observed. The areas exceeding 55°C are 39 mm<sup>2</sup> for 30W - 60 s and 112 mm<sup>2</sup> for 60 W - 60 s in  
 223 muscle, 3 mm<sup>2</sup> for 30 W - 60 s and 30 mm<sup>2</sup> for 60 W - 60 s in fat, for the 15 mm case; 43 mm<sup>2</sup> for 30 W  
 224 - 60 s and 114 mm<sup>2</sup> for 60 W - 60 s in muscle, and 4 mm<sup>2</sup> for 30 W - 60 s and 31 mm<sup>2</sup> for 60 W - 60 s  
 225 in fat, for the 5 mm case. The ablation areas calculated both at 30 W and 60 W power setting for the  
 226 homogeneous scenario and for each muscle-fat interface scenario are reported in Table 2.

227  
 228

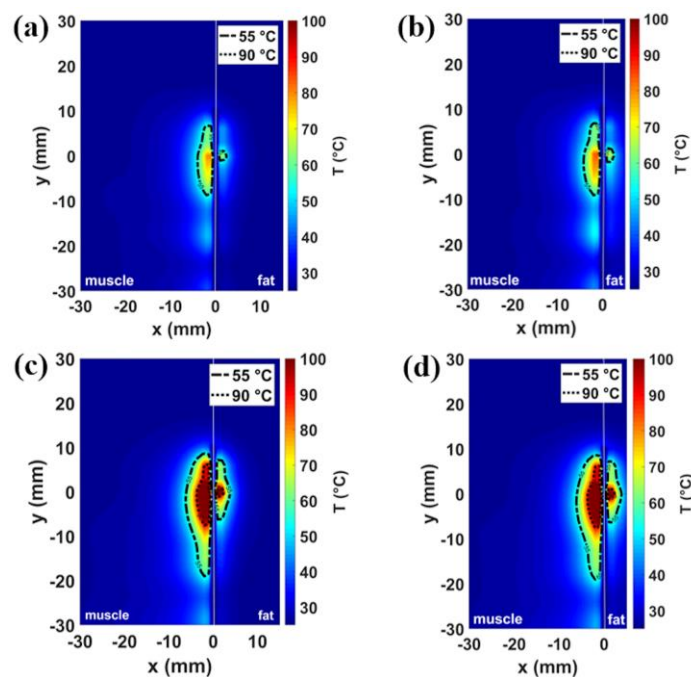


Figure 4: Simulated temperature patterns in muscle-fat interface scenario shown in a coronal plane with reference to the antenna feed for two different fat layer widths: 15 mm (a,c) and 5 mm (b,d). Two different power-time settings are reported: 30 W-60s (a,b); 60W-60s (c,d).

Table 2: Areas of ablation zones calculated at 30 W (first line) and at 60 W (second line) in muscle in the case of homogeneous scenario and both in muscle and in fat in the interface scenario considering 15 mm, 10 mm and 5 mm fat layer width.

Settings		Area enclosed in 55°C contour						
		Homogeneous	Interface Fat width: 15 mm		Interface Fat width: 10 mm		Interface Fat width: 5 mm	
P (W)	t (s)	Muscle*	Fat	Muscle	Fat	Muscle	Fat	Muscle
30	60	10 mm <sup>2</sup>	3 mm <sup>2</sup>	39 mm <sup>2</sup>	3 mm <sup>2</sup>	41 mm <sup>2</sup>	4 mm <sup>2</sup>	43 mm <sup>2</sup>
60	60	65 mm <sup>2</sup>	30 mm <sup>2</sup>	112 mm <sup>2</sup>	31 mm <sup>2</sup>	117 mm <sup>2</sup>	31 mm <sup>2</sup>	114 mm <sup>2</sup>

\* in the case of homogeneous scenario, the values reported refer to one side of the muscle.

229 Figure 5 shows the results obtained for 30 W- 60 s (figures (a-b)) and 60 W - 60 s (figures (c-d))  
 230 settings accounting for the influence of an antenna misalignment of 1.5 mm in fat (figures (a-c)) or  
 231 muscle (figures (b-d)). In the case of 1.5 mm displacement of the antenna in fat, the longitudinal axis  
 232 of the antenna is positioned inside the fat layer, thus the antenna is immersed in fat. In the case of 1.5  
 233 shift of the antenna in muscle, the longitudinal axis of the antenna is positioned inside the muscle  
 234 region, thus the antenna is immersed in muscle.

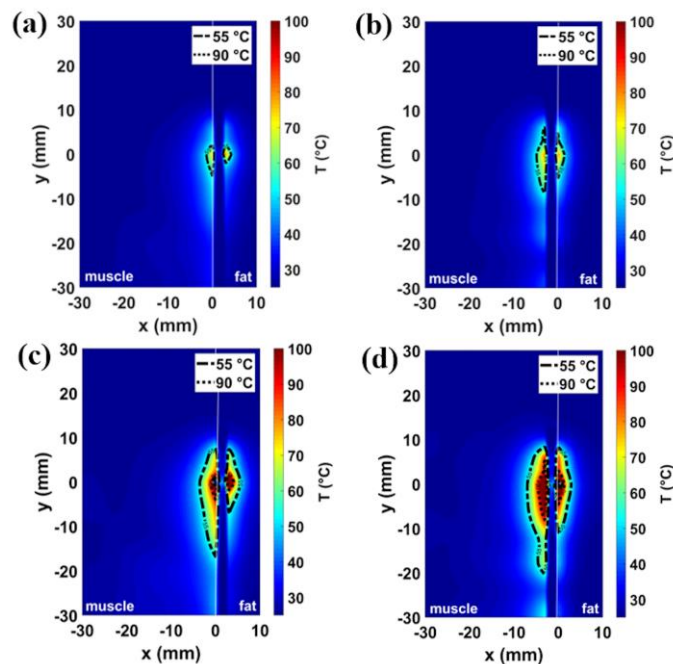


Figure 5: Simulated temperature patterns in muscle-fat interface scenario shown in a coronal plane with reference to the antenna feed for 1.5 mm displacement of the antenna along x-axis in fat (a,c) and in muscle (b,d). Two different power-time settings are reported: 30 W-60s (a,b); 60W-60s (c,d).

235 In the case of 1.5 mm misalignment in fat, the sizes of the ablation zones are 7 mm<sup>2</sup> in muscle  
 236 and 4 mm<sup>2</sup> in fat for 30 W power setting and 67 mm<sup>2</sup> in muscle and 28 mm<sup>2</sup> in fat, for 60 W setting.  
 237 For the antenna misalignment in muscle, the areas exceeding 55°C are 20 mm<sup>2</sup> in muscle and 10 mm<sup>2</sup>  
 238 in fat for 30 W, 89 mm<sup>2</sup> in muscle and 47 mm<sup>2</sup> in fat, for 60 W. Compared to the scenario of perfect  
 239 alignment of the antenna along the interface between fat and muscle (Figure 3), a smaller asymmetry  
 240 can be observed: the ablation areas in muscle are only two times the ablation areas in fat. For both

241 the misalignment scenarios, a smaller impact of the fat-muscle interface on the reflection of the  
 242 electromagnetic energy in the target tissue is observed.

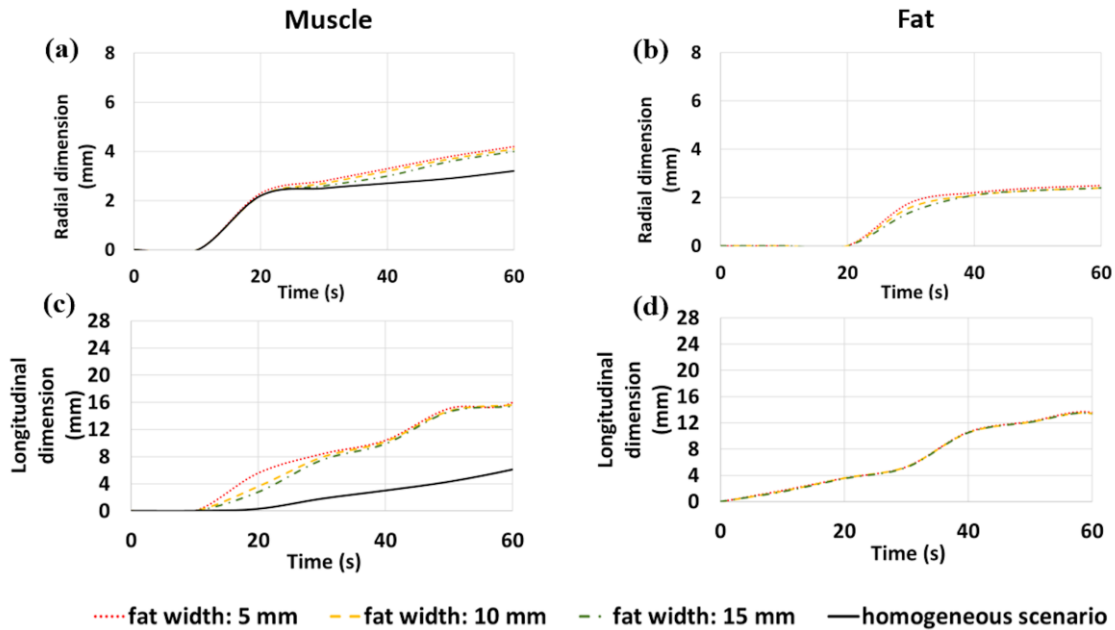


Figure 6: Variations of the radial (a,b) and longitudinal (c,d) dimensions of the ablation zone over time at 30 W in muscle (a,c) and in fat (b,d). Interface scenarios (red line: 5 mm wide fat case; yellow line: 10 mm wide fat case; green line: 15 mm wide fat case) and homogenous scenario (black line) are compared.

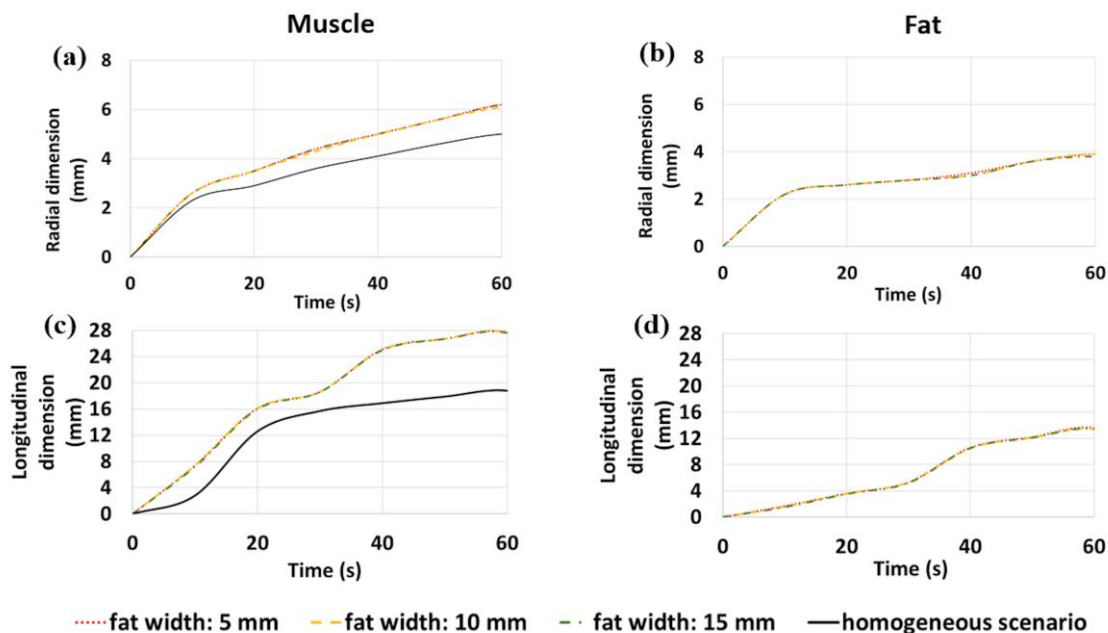


Figure 7: Variations of the radial (a,b) and longitudinal (c,d) dimensions of the ablation zone over time at 60 W in muscle (a,c) and in fat (b,d). Interface scenarios (red line: 5 mm wide fat case; yellow line: 10 mm wide fat case; green line: 15 mm wide fat case) and homogenous scenario (black line) are compared.

243 The numerical results presented above (Figure 2 to 4) are compared in Figure 6 and Figure 7 in  
 244 terms of variations of the radial and longitudinal dimensions of the ablation zone (i.e. the area where  
 245 the temperatures is above 55°C) over the time of the ablation procedure (up to 60 s, at 10 s time step).  
 246 The dimensions are reported for both fat and muscle of the interface scenario, for each fat width  
 247 considered (5, 10, 15 mm) and for the homogenous scenario. The increases in the radial and

248 longitudinal dimensions of the ablation zone over time in muscle for each one of the different fat  
 249 layer width investigated can be observed in comparison with the homogeneous scenario. First, it can  
 250 be noticed that the growth rate of the ablation zone is independent of the fat width in both tissues.

251 In the case of the 30 W setting (Figure 6), the ablation zone starts to form only after 10 s in muscle  
 252 and 20 s in fat. The radial dimension of the ablation zone in muscle at the interface with fat starts to  
 253 increase after 20 s with respect to the homogeneous scenario; while such difference becomes sizeable  
 254 after about 40 s. In fat, the radial dimension of the ablation zone reaches the steady state after 40 s.  
 255 Longitudinally, the growth of the ablation zone in fat is limited during the whole procedure; while a  
 256 substantial increase of the ablation zone in muscle with respect to the homogeneous case is observed.  
 257 In particular, the longitudinal dimension in muscle grows of about 0.3 mm/s steadily from 10 s to 40  
 258 s. At 40 s, a change in the slope of the curve occurs and an increase of about 5 mm is observed at 50 s  
 259 (about 0.5 mm/s), before reaching a plateau.

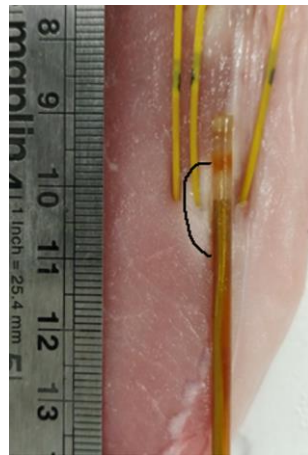


Figure 8: Section of a MTA obtained in *ex vivo* porcine sample: the applicator (MW antenna) and fibre optic sensors placement in the tissue is showed. The antenna is placed at the visible interface between the muscle and the fat, and the ablation zone obtained in the muscle is marked. The ablation zone is not visible in fat.

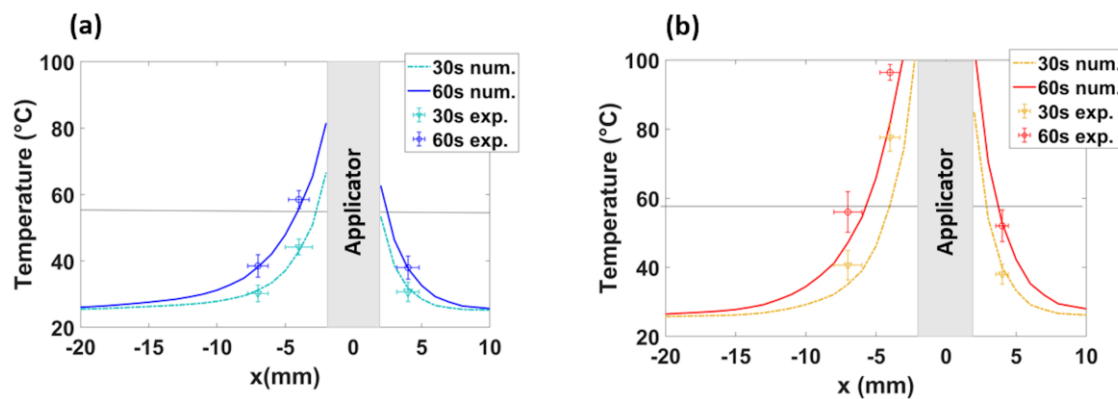


Figure 9: Numerical (num.) and experimental (exp.) values of temperature over the radial distance from the MW antenna axis (applicator) both in muscle and fat at 30s and 60s for 30W (a) and 60W (b). The horizontal line highlights the temperature threshold at 55°C.

260 In the case of the 60 W setting (Figure 7), higher values of the radial dimension of the ablation  
 261 zone in muscle compared to the homogeneous scenario are visible after 10 s; this difference remains  
 262 constant over time. In fat, the radial dimension of the ablation zone reaches a plateau after 10 s and  
 263 slowly starts increasing again after 40 s. In contrast to the 30 W case, the growth of the ablation zone  
 264 along the longitudinal dimension is noticeable in fat at 60 W. Longitudinally the ablation zone in fat  
 265 is limited for the first 30 s; then, at 30 s a change in the slope of the curves both in fat and muscle leads  
 266 to a substantial increase in the ablation zone length over the following 30 s (up to the end of the

267 procedure). A similar change of slope can be observed in muscle at the same time (at 30 s).  
268 Finally, the numerical results have been experimentally validated. Experimental MTAs (N=10, five at  
269 30W for 60 s and five at 60 W for 60 s) were obtained exploiting the natural muscle-fat interface of *ex*  
270 *vivo* porcine tissue. The MW antenna was placed adjacent to the interface between muscle and fat;  
271 and the increase of temperature at different radial distances from the antenna axis was monitored  
272 with fiber optic sensors placed in fat at  $4 \pm 1$  mm from the antenna axis and in muscle at  $4 \pm 1$  mm  
273 and at  $7 \pm 1$  mm from the antenna axis (as shown in Figure 8). The thermal profiles observed  
274 numerically at 30 s and 60 s are compared with the experimental values obtained from the fiber optic  
275 sensors at 30 s and 60 s during the MTA procedure in Figure 9 for 30 W (a) and 60 W (b). The  
276 temperature increase as a function of the radial distances from the antenna feed is reported. The  
277 experimental data well match the numerical trends and the impact of the differences in electrical and  
278 thermal characteristics between two tissue is visible.

#### 279 4. Discussion

280 In this work the influence of the fat layer tissue on the size and shape of microwave ablation  
281 zones as well as on the temperature increase is characterized. The aim of the study was to investigate  
282 the role of the fat layer, characterized by dielectric and thermal properties lower than the target tissue,  
283 as biological “shield” of the heating pattern; i.e. the ability of fat to reflect the electromagnetic power  
284 into the tissue target while reducing the heating in the opposite direction. This approach could be  
285 exploited for the minimally invasive treatment of peripheral lesions (e.g. in liver or kidney) and  
286 adenomas affecting adrenal glands, where an interface between fat and the target tissue is available  
287 and **accessible with the antenna parallel to the interface** [32]. Such interface (fat-target tissue) can be  
288 easily detected by imaging techniques, used to align the antenna and perform a side-firing ablation  
289 without the need for the clinicians to carefully manage the antenna orientation (as with directional  
290 antennas). A similar concept has been adopted in [20], for the MTA treatment of spinal metastatic  
291 tumors where the low dielectric properties of the adjacent vertebral bone facilitated the local control  
292 of the ablation zone in the surrounding neural structures.

293 An investigative numerical study is proposed in this work exploiting an exemplificative and  
294 dielectrically conservative interface model (muscle-fat) and a monopole antenna. The numerical  
295 analysis was validated in an *ex vivo* porcine model with a monopole antenna prototyped in-house.  
296 First, the ability of the antenna to effectively transfer the power to the tissues was ensured. A  
297 reflection coefficient below -10 dB over a sufficiently large frequency interval centered at the  
298 operating frequency of 2.45 GHz was secured, in order to guarantee satisfying operational  
299 performance independently of the variations in dielectric properties of the tissue.

300 The optimized antenna was adopted to conduct the numerical study both in the muscle-fat  
301 interface model and in the homogeneous model. Comparing the results obtained in the homogenous  
302 model (Figure 2) with the results obtained in the muscle-fat interface model (Figure 3), asymmetry in  
303 the heating distributions are observed at the interface between the adipose layer and the muscle layer.  
304 **The asymmetric heating patterns observed for each power and time setting (Figure 3) are the result**  
305 **of the different interaction mechanisms between fat and muscle with the EM field. Because of the**  
306 **lower values in relative permittivity and effective conductivity, ablation zones (i.e. the area where a**  
307 **temperature at least equal to 55 °C is achieved) in the fat layer are observed to be constantly smaller**  
308 **and more spherical compared to muscle layer, independently from the thickness of the fat layer**  
309 **(Figure 4). Different ratios of asymmetry were observed for the two power settings investigated: the**  
310 **ablation zone in fat was at least ten times smaller than in muscle for the lower power tested (30 W),**  
311 **and about four time for the higher power (60 W).**

312 **The high contrast in terms of relative permittivity and effective conductivity between fat and**  
313 **muscle at the interface induces higher levels of energy, and consequently of heating, in the muscle**  
314 **layer in proximity to the applicator, when compared to the homogeneous scenario. Accordingly, it is**  
315 **conceivable that the fat layer not only shields the electromagnetic radiation, but also reflects the**  
316 **electromagnetic power into the adjacent tissue characterized by higher values of relative permittivity**  
317 **and effective conductivity. The electromagnetic field reflected in muscle, at the interface with fat, is**

318 redistributed along the antenna axis inducing a noticeable, yet not desirable, elongation of the  
319 ablation zone in muscle. In the used applicator, back-heating along the antenna axis is limited only  
320 by the active cooling that balances the temperatures increase. Thus, such increase in the longitudinal  
321 direction would be expected, but could be easily minimized adopting a different antenna design  
322 [33,34].

323 Moreover, different rates of coagulation (depicted in Figure 6 and 7 by the edge of the ablation  
324 zone, i.e. by the 55 °C threshold) were observed for the two different levels of input power (30 and 60  
325 W) in muscle in the interface scenario, when compared with the homogeneous scenario. In particular,  
326 a sequence of saturations (plateau) of the monotonic increase of the length of the ablated zone  
327 (longitudinal dimension of Figure 6 and 7) have been observed at different times for the two different  
328 power settings proposed. Both at 30 W and 60 W, the change in the slope of the curves related to the  
329 longitudinal dimension of the ablation zone occurs when the radial dimension of the ablation zone  
330 in muscle in the interface scenario becomes higher than the equivalent dimension obtained in the  
331 homogeneous scenario. Therefore, at 40 s in the case of 30 W and at 30 s in the case of 60 W, the  
332 ablation length in muscle increases faster than the corresponding one in the homogenous scenario,  
333 inducing the elongation of the ablation zones. A similar behavior has been observed for MTA in thin  
334 tissue samples [35]. These differences suggest that the success of this approach is highly dependent  
335 on the power and time settings of the procedure; lower power and shorter ablation time enable more  
336 controlled ablation zones and promising results. Pulsed protocols could be optimal for this approach  
337 in order to allow the fat tissue to recover from the heat stress and retrieve its shielding capabilities.  
338 The higher dielectric properties (i.e. relative permittivity and effective conductivity) of muscle enable  
339 higher deposition of the electromagnetic power and temperature increases compared to fat; while,  
340 the different thermal conductivities between fat and muscle determine the steepness of the  
341 temperature increase. Thus, the reduced heating in the adipose tissue is also due to the lower values  
342 of thermal conductivity and thermal diffusivity (i.e. ratio between thermal conductivity and  
343 volumetric heat capacity). In particular, the lower diffusivity of the fat tissue is responsible for the  
344 slower propagation of the heat beyond the area of active heating due to the direct deposition of the  
345 electromagnetic power.

346 Antenna misalignment was investigated to account for a scenario of poor spatial resolution  
347 provided by the imaging technique currently used [36]. Asymmetric heating patterns were  
348 numerically obtained also in the case of a not perfect alignment of the antenna at the interface  
349 between fat and muscle, even if the difference between the two adjacent ablation zones was visibly  
350 reduced (Figure 5). A **two-fold** asymmetry was observed independently from the power applied  
351 (instead of the ten and **four-fold** observed for the perfect alignment at 30 and 60 W respectively). The  
352 precise orientation of the antenna is not strictly required to exploit the shielding effect induced by the  
353 fat presence, but it should be considered to properly predict the resulting dimension of the ablated  
354 zone.

355 Finally, the numerical results were successfully validated experimentally. The temperature  
356 profiles monitored in both tissues (Figure 9) are in good agreement with the patterns predicted by  
357 the thermal simulations. A minimal discrepancy between the numerical and experimental data can  
358 be observed in muscle only for the 60 W MTA setting. This mismatch could be likely related to the  
359 transient deformations of the tissue in proximity to the antenna; such tissue deformation (i.e.  
360 shrinkage) was not considered in the numerical model [37,38]. Moreover, the thermal lesions  
361 obtained from the numerical simulations are calculated considering the minimum temperature equal  
362 to 55 °C, i.e. an approximated value. Such value was chosen in this study considering that the  
363 minimum temperature to obtain the coagulation effect of the target tissue is reasonably within 50 –  
364 60 °C [1]. However, this value can slightly vary with the tissue types and due to different initial  
365 conditions (e.g. initial temperature) of the tissue.

## 366 5. Conclusions

367 This work analyses the impact of the fat layer on the coagulated zone achievable through  
368 microwave thermal ablation procedures. Results show that, when a layer of fat tissue lies at the

369 interface with a tissue characterized by higher dielectric properties (muscle tissue was used in this  
370 study), the area of the ablation zone increases with respect to the homogeneous scenario (only  
371 muscle). Such increase is caused by dielectric contrast between the two adjacent tissues and the  
372 consequent reflection of the electromagnetic field into the tissue characterized by higher dielectric  
373 properties (i.e. the target) compared to the shield tissue (i.e. fat). The findings of this study highlight  
374 the potential advantage to exploit the natural fat layer at the interface with potential targets such as  
375 liver, kidneys, adrenal glands to focus most part of the electromagnetic field into the target tissue.

376

377 **Author Contributions:** Conceptualization, A.B., G.R. and L.F.; methodology, A.B., G.R. and L.F.; software, A.B.  
378 and G.R.; validation, A.B. and L.F.; formal analysis, A.B.; investigation, A.B. and L.F.; resources, M.O.; data  
379 curation, A.B.; writing—original draft preparation, A.B.; writing—review and editing, L.F. G.R. and M.O.;  
380 visualization, A.B. and L.F.; supervision, L.F.; project administration, M.O.; funding acquisition, M.O. All  
381 authors have read and agreed to the published version of the manuscript.

382 **Funding:** The research leading to these results has received funding from the European Research Council under  
383 the European Union’s Horizon 2020 Programme (H2020)/ERC grant agreement n.637780 and ERC PoC Grant  
384 REALTA n.754308. This publication has emanated from research conducted with the financial support of Science  
385 Foundation Ireland (SFI) and is co-funded under the European Regional Development Fund under Grant  
386 Number 13/RC/2073. This project has received funding from the European Union Horizon 2020 research and  
387 innovation programme under the Marie Skłodowska-Curie grant agreement No 713690.

388 **Conflicts of Interest:** The authors declare no conflict of interest. The funders had no role in the design of the  
389 study; in the collection, analyses, or interpretation of data; in the writing of the manuscript, or in the decision to  
390 publish the results.

391

## 392 References

- 393 [1] Ahmed M.; Brace C.L.; Lee F. T.; Goldberg S. N. Principles of and advances in percutaneous ablation.  
394 *Radiology* **2011**, *258*, 351–369.
- 395 [2] Brace C. Thermal tumour ablation in clinical use. *IEEE Pulse* **2011**, *2*, 28–38.
- 396 [3] Dong B.; Yu J.; Liang P. Microwave ablation: principles and techniques. *Microwave ablation treatment of*  
397 *solid tumors*. 1st ed.; Liang P.; Yu X.L.; Yu J.; Editor 2, B., Eds.; Springer Dordrecht Heidelberg, Germany,  
398 2015; pp. 3–13.
- 399 [4] Lubner M.G.; Brace C. L.; Hinshaw J. L.; Lee F. T. Microwave tumour ablation: mechanism of action,  
400 clinical results and devices. *J. Vasc. Interv. Radiol.* **2010**, *21*, 192–203.
- 401 [5] Chu K. F.; Dupuy D. E. Thermal ablation of tumours: biological mechanisms and advances in therapy.  
402 *Nat. Rev. Cancer* **2014**, *14*, 199–208.
- 403 [6] Goldberg S.N.; Gazelle G.S.; Mueller P. R. Thermal Ablation Therapy for Focal Malignancy. *Am. J.*  
404 *Roentgenol.* **2000**, *174*, 323–331.
- 405 [7] Curto S.; Taj-Eldin M.; Fairchild D.; Prakash P. Microwave ablation at 915 MHz vs 2.45 GHz: a theoretical  
406 and experimental investigation. *Med. Phys.* **2015**, *42*, 6152–6161.
- 407 [8] Lopresto V.; Pinto R.; Farina L.; Cavagnaro M. Treatment planning in microwave thermal ablation :  
408 clinical gaps and recent research advances. *Int. J. Hyperther.* **2017**, *33*, 83–100.
- 409 [9] Liu Y.; Zheng Y.; Li S.; Li B.; Zhang Y.; Yuan Y. Percutaneous microwave ablation of larger hepatocellular  
410 carcinoma. *Clin. Radiol.* **2013**, *68*, 21–26.
- 411 [10] Wells S.A.; Hinshaw J.L.; Lubner M.G.; Ziemlewicz T.J.; Brace C.L.; Lee F.T. Liver ablation: best practice.  
412 *Radiol. Clin. North Am.* **2015**, *53*, 933–971.
- 413 [11] Meloni M.F.; Chiang J.; Laeseke P.F.; Dietrich C.F.; Sannino A.; Solbiati M.; Nocerino E.; Brace C.L.; Lee  
414 F.T. Microwave ablation in primary and secondary liver tumours: technical and clinical approaches. *Int.*  
415 *J. Hyperther.* **2017**, *33*, 15–24.
- 416 [12] Klapperich M.E.; Abel E.J.; Ziemlewicz T.J.; Best S.; Lubner M.G.; Nakada S. Y.; Hinshaw J.L.; Brace C.L.;  
417 Lee F.T; Wells S.A. Effect of tumor complexity and technique on efficacy and complications after  
418 percutaneous microwave ablation of stage T1a renal cell carcinoma: a single-center, retrospective study,”

- 419 *Radiology* **2017**, *284*, 272–280.
- 420 [13] Higgins L.J.; Hong K. Renal ablation techniques: state of the art. *Am. J. Roentgenol.* **2015**, *205*, 735–741.
- 421 [14] Alexander E.; Dupuy D.E. Lung cancer ablation: technologies and techniques. *Semin. Intervent. Radiol.*  
422 **2013**, *30*, 141–150.
- 423 [15] Kostrzewa M.; Diezler P.; Michaely H.; Rathmann N.; Attenberger U.I.; Schoenberg S.O.; Diehl S.J.  
424 Microwave ablation of osteoid osteomas using dynamic MR imaging for early treatment assessment:  
425 Preliminary experience. *J. Vasc. Interv. Radiol.* **2014**, *25*, 106–111.
- 426 [16] McWilliams B.T.; Schnell E.E.; Curto S.; Fahrback T.M.; Prakash P. A Directional Interstitial Antenna for  
427 Microwave Tissue Ablation: Theoretical and Experimental Investigation. *IEEE Trans. Biomed. Eng.* **2015**,  
428 *62*, 2144–2150.
- 429 [17] Mohtashami Y.; Hagness S.C.; Behdad N. A Hybrid Slot/Monopole Antenna with Directional Heating  
430 Patterns for Microwave Ablation. *IEEE Trans. Antennas Propag.*, 2017, *65*, 3889–3896.
- 431 [18] Sebek J.; Curto S.; Bortel R.; Prakash P. Analysis of minimally invasive directional antennas for  
432 microwave tissue ablation. *Int. J. Hyperther.* **2017**, *33*, 51–60.
- 433 [19] Li M.; Yu X.; Liang P.; Liu F.; Dong B.; Zhou P. Percutaneous microwave ablation for liver cancer adjacent  
434 to the diaphragm. *Int. J. Hyperther.*, **2012**, *28*, 218–226.
- 435 [20] Kastler A.; Alnassan H.; Aubry S.; Kastler B.; Microwave thermal ablation of spinal metastatic bone  
436 tumors. *J. Vasc. Interv. Radiol.*, **2014**, *25*, 1470–1475.
- 437 [21] Gabriel C.; Gabriel S.; Corthout E. The dielectric properties of biological tissues: I. Literature survey.  
438 *Phys. Med. Biol.* **1996**, *41*, 2231–2249.
- 439 [22] Hasgall P.A.; Di Gennaro F.; Baumgartner C.; Neufeld E.; Lloyd B.; Gosselin M.C.; Payne D.;  
440 Klingenböck A. IT'IS Database for thermal and electromagnetic parameters of biological tissues  
441 [itis.swiss/database](http://itis.swiss/database).
- 442 [23] Ruvio G.; Eaton-Evans J.; Shahzad A.; O'Halloran M. Numerical evaluation of microwave thermal  
443 ablation to treat small adrenocortical masses. *Int. J. RF Microw. Comput. Eng.*, **2018**, *28*, 1–8.
- 444 [24] Bottiglieri A.; Farina L.; Shahzad A.; O'Loughlin D.; O'Halloran M.; Elahi M.A. Microwave Thermal  
445 Ablation: Focusing energy in target tissue using fat layer. *13th Eur. Conf. Antennas Propagation, EuCAP*  
446 **2019**, 1–4.
- 447 [25] Pennes H.H. Analysis of tissue and arterial blood temperatures in the resting human forearm. *J. Appl.*  
448 *Physiol.* **1948**, *1*, 93–122.
- 449 [26] La Gioia A.; Salahuddin S.; O'Halloran M.; Porter E. Quantification of the sensing radius of a coaxial  
450 probe for accurate interpretation of heterogeneous tissue dielectric data. *IEEE J. Electromagn. RF*  
451 *Microwaves Med. Biol.*, **2018**, *2*, 145–153.
- 452 [27] Ruvio G.; Farina L.; Bottiglieri A.; Eaton-Evans J.; Elahi M.A.; O'Halloran M.; Pinto R.; Lopresto V.;  
453 Cavagnaro M. Comparison of coaxial open-ended probe based dielectric measurements on ex-vivo  
454 thermally ablated liver tissue. *13th Eur. Conf. Antennas Propagation, EuCAP 2019*, **2019**, 5–8.
- 455 [28] Micro-Coax, MIL-DTL-17 Approved Cables, Component Distributions, Inc., 1–8.
- 456 [29] Cavagnaro M.; Pinto R.; Lopresto V. Numerical models to evaluate the temperature increase induced by  
457 ex vivo microwave thermal ablation. *Phys. Med. Biol.* **2015**, *60*, 3287–3311.
- 458 [30] Lopresto V.; Pinto R.; Lovisolò G.A.; Cavagnaro M. Changes in the dielectric properties of ex vivo bovine  
459 liver during microwave thermal ablation at 2.45 GHz. *Phys. Med. Biol.*, **2012**, *57*, 2309–2327.
- 460 [31] Chiang J.; Cristescu M.; Lee H.M.; Moreland A.; Hinshaw J.L.; Lee F.T.; Brace C.L. Effects of microwave  
461 ablation on arterial and venous vasculature after treatment of hepatocellular carcinoma. *Radiology* **2016**,  
462 *281*, 617–624.
- 463 [32] Donlon P.T.; Hojjatollah F.; Beard W.L.; Heflin L.; Cox W.; Bloomberg B.; Lillich J.D.; Ganta C.K.;  
464 O'Sullivan G.J.; Ruvio G.; O'Shea P.M.; O'Halloran M.; Prakash P.; Denedy M.C.; Using microwave  
465 thermal ablation to develop a subtotal, cortical-sparing approach to the management of primary  
466 aldosteronism. *Int. J. Hyperther.* **2019**, *36*, 905–914.
- 467 [33] Longo I.; Gentili G.B.; Cerretelli M.; Tosoratti N. A coaxial antenna with miniaturized choke for  
468 minimally invasive interstitial heating. *IEEE Trans. Biomed. Eng.* **2003**, *50*, 82–88.
- 469 [34] Farina L.; De Marco A.J.; Bottiglieri A.; Ruvio G.; Eaton-Evans J.; Denedy M.C.; Elahi M.A.; O'Halloran  
470 M. Microwave ablation antenna for functional adenomas in the Adrenal Gland. *2019 Photonics &*

- 471 *Electromagnetics Research Symposium - Spring (PIERS-Spring).*
- 472 [35] Cavagnaro M.; Amabile C.; Cassarino S.; Tosoratti N.; Pinto R.; Lopresto V. Influence of the target tissue  
473 size on the shape of ex vivo microwave ablation zones. *Int. J. Hyperth.* **2015**, *31*, 48–57.
- 474 [36] Strigari L.; Minosse S.; D'Alessio D.; Farina L.; Cavagnaro M.; Cassano B.; Pinto R.; Vallati G.; Lopresto  
475 V. Microwave thermal ablation using CT-scanner for predicting the variation of ablated region over  
476 time: Advantages and limitations. *Phys. Med. Biol.*, **2019**, *64*, 115–129.
- 477 [37] Liu D.; Brace C.L. Numerical simulation of microwave ablation incorporating tissue contraction based  
478 on thermal dose. *Phys. Med. Biol.* **2017**, *62*, 2070–2086.
- 479 [38] Lopresto V.; Pinto R.; Farina L.; Cavagnaro M. Microwave thermal ablation: Effects of tissue properties  
480 variations on predictive models for treatment planning. *Med. Eng. Phys.* **2017**, *46*, 63–70.
- 481